

Calculation of the incremental stress-strain relation of a polygonal packing

F. Alonso-Marroquin and H. J. Herrmann
 ICA1, University of Stuttgart,

Pfaffenwaldring 27
 70569 Stuttgart, Germany
 (February 1, 2008)

The constitutive relation of the quasi-static deformation on two dimensional packed samples of polygons is calculated using molecular dynamic simulations. The stress values at which the system remains stable are bounded by a failure surface, that shows a power law dependence on the pressure. Below the failure surface, non linear elasticity and plastic deformation are obtained, which are evaluated in the framework of the incremental linear theory. The results shows that the stiffness tensor can be directly related to the micro-contact rearrangements. The plasticity obeys a non-associated flow rule, with a plastic limit surface that does not agree with the failure surface.

I. INTRODUCTION

The non linear and irreversible behavior of soils has been described by different constitutive theories [1,2]. Here the stress - strain relation is postulated using a certain number of material parameters that are measured in experimental tests. In practice, the constitutive relations can be constructed directly, taking samples with the same macroscopical state, and measuring in each one the incremental strain that results from the application of a specific stress increment [3]. However, such tests are difficult to perform, because they require the fabrication of many samples with identical material properties.

Numerical simulations result as an alternative to the solution of this problem. They allow to develop different tests on identically generated samples and provide detailed information about micro-mechanical rearrangements during the loading process. Usually, disks or spheres are used to capture the granularity of the sample [4,5]. Although the simplicity of their geometry allows to reduce the computer time of calculations, they do not provide a detailed description of realistic granular textures.

We present here a two dimensional discrete model that takes into account the diversity of shapes of the grains in the soils. The granular samples consist of randomly generated polygons. As presented by Tillemans [6], The interaction between the polygons could be handled letting the polygons interpenetrate each other and calculating the force as a function of their overlap. This approach has been successfully applied to model different processes, like fragmentation [7] and strain localization [6]. A suitable contact force law is introduced in Sect.IIA, that attempts to combine the Hertz contact law with the Coulomb friction criterion for quasi-static deformation.

The incremental stress-strain relation was calculated performing different stress increments on the same sample, and measuring the corresponding strain response. The stress is applied on the boundary through a flexible

membrane that surrounds the sample. The modeling of such a membrane, whose details are given in Sect. IIB, results more complex than rigid walls, However, it results more advantageous than walls, because it allows to implement a stress-controlled condition without any restriction in the deformation of the boundary.

II. MODEL

The polygons of this model are generated using a simple version of the Voronoi tessellation: First we set a random point in each cell of a regular square lattice. Then each polygon is constructed assigning to each point that part of the plane that is nearer to it than to any other point. Each polygon is subjected to interparticle contact forces and boundary forces that are inserted in Newton's equation of motion.

A. Contact force

Usually, the interaction between two solid bodies in contact is described by a force applied on the flattened contact surface between them. Given two polygons in contact, such surface is obtained from the geometrical construction shown in Fig. 1. The points C_1 and C_2 result from the intersection between the edges of the polygons. The contact surface is taken as the segment that lies between those points. The vector $\vec{S} = \vec{c_1c_2}$ defines an intrinsic coordinate system at the contact (\hat{t}, \hat{n}) , where $\hat{t} = \vec{S}/|\vec{S}|$ and \hat{n} is perpendicular to it. The deformation length is given by $\delta = a/|\vec{S}|$ where a is the overlap area between the polygons. \vec{l} is the branch vector, that connects the center of mass of the polygon to the point of application of the contact force, that is supposed to be the center of mass of the overlap area.

The normal elastic force is taken proportional to the deformation length as $f_n^e = k_n \delta$; the tangential force is calculated from the simplified Coulomb friction law,

with a single friction coefficient $\mu_s = \mu_d = \mu$. Here μ_s is the static and μ_d the dynamic friction coefficient. This tangential force is implemented by an elastic spring $f_t^e = -k_t \xi$, where ξ grows linearly with the tangential displacement of the contact, whenever $|f_t^e| < \mu f_n^e$. We used the straightforward calculation of ξ proposed by Brendel [8]:

$$\xi(t) = \int_0^t v_n(t') \Theta(f_n^e(t') - \mu|f_t^e(t')|) dt' \quad (1)$$

where Θ is the Heaviside function and \vec{v} is the relative velocity at the contact, that depends on the linear velocity \vec{v}_i and angular velocity $\vec{\omega}_i$ of the particles in contact according to:

$$\vec{v} = \vec{v}_i - \vec{v}_j - \vec{\omega}_i \times \vec{\ell}_i + \vec{\omega}_j \times \vec{\ell}_j \quad (2)$$

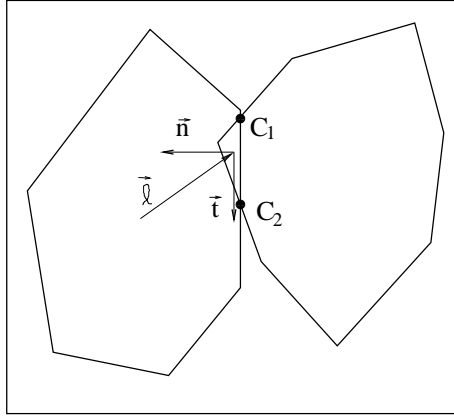


FIG. 1. Contact surface as defined from the geometry of overlap.

B. Boundary Forces

Let us now discuss how to apply the stress on the sample. One way to do that, would be to apply a perpendicular force on each edge of the polygons belonging to the external contour of the sample. Actually this does not work, because this force will act on all the fjords of the boundary. It produces an uncontrollable growth of cracks that with time ends up destroying the sample. Thus, results necessary to introduce a flexible membrane in order to restrict the boundary points that are subjected to the external stress.

The algorithm to identify the boundary is rather simple. The lowest vertex p from all the polygons of the sample is chosen as the first point of the boundary list b_1 . In Fig. 2 P is the polygon that contains p , and $q \in P \cap Q$ is the first intersection point between the polygons P and Q in counterclockwise orientation with respect to p . Starting from p , the vertices of P in counterclockwise orientation are included in the boundary list

until q is reached. Next, q is included in the boundary list. Then, the vertices of Q between q and the next intersection point $r \in Q \cap R$ in the counterclockwise orientation are included into the list. The same procedure is applied until one reaches the lowest vertex p again. This is a very fast algorithm, because it only makes use of the contact points between the polygons, which are previously calculated to obtain the contact force.

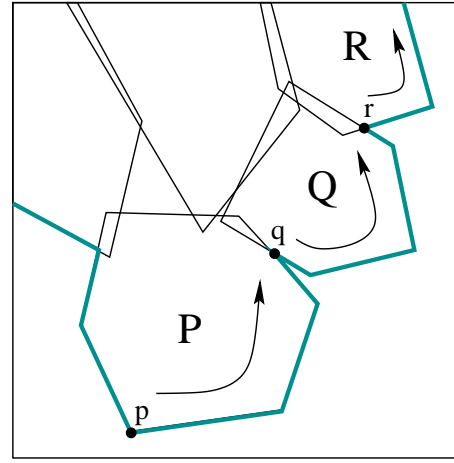


FIG. 2. Algorithm used to find the boundary.

The set of points that are in contact with the membrane are selected using a recursive algorithm. It is initialized with the vertices of the smallest convex polygon that encloses the boundary. (see Fig. 3). The lowest point of the boundary is selected as the first vertex of the polygon $m_1 = b_1$. The second one m_2 is the boundary point b_i that minimizes the angle $\angle(\vec{b}_1 \vec{b}_i)$ with respect to the horizontal. The third one m_3 is the boundary point b_i such that the angle $\angle(\vec{m}_2 \vec{b}_i, \vec{m}_1 \vec{m}_2)$ is minimal. The algorithm is recursively applied until the lowest vertex m_1 is reached again.

The points of the boundary are iteratively included in the list m_i using the bending criterion proposed by Åström [10]: For each pair of consecutive vertices of the membrane $m_i = b_i$ and $m_{i+1} = b_j$ we choose that point from the subset $\{b_k\}_{i \leq k \leq j}$ that maximizes the bending angle $\theta_b = \angle(\vec{b}_k \vec{b}_i, \vec{b}_k \vec{b}_j)$. This point is included into the list, whenever $\theta_b \geq \theta_{th}$. Here θ_{th} is a threshold angle for bending. This algorithm is repeatedly applied until there are not more points satisfying such bending condition.

The final result gives a set of segments $\{\vec{m}_i \vec{m}_{i+1}\}$ lying on the boundary of the sample. In order to apply the boundary forces, those segments are divided into two groups: A-type segments are those that coincide with an edge of a boundary polygon; B-type segments connect the vertices of two different boundary polygons.

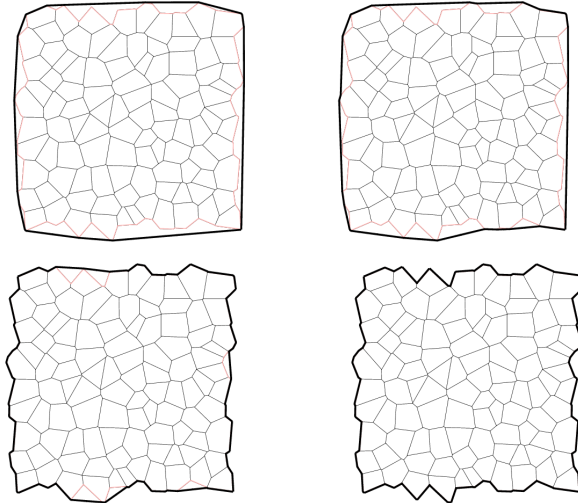


FIG. 3. Membrane obtained with threshold bending angle $\theta_{th} = \pi, 3\pi/4, \pi/2$ and $\pi/4$, the first one corresponds to the minimum convex polygon that encloses the sample.

On each segment of the membrane $\overrightarrow{m_i m_{i+1}}$ a force $f_i = \sigma_i N_i$ is applied, where σ_i is the local stress and N_i is the 90° counterclockwise rotation of $\overrightarrow{m_i m_{i+1}}$. This force is transmitted to the polygons in contact with it: if the segment is A-type, this force is applied in its midpoint; If the segment is B-type, half of the force is applied at each one of the vertices connected by this segment.

C. Molecular dynamic simulation

Before we implement the numerical solution of Newton's equations it is convenient to make a dimensional analysis of the parameters. In such way we can keep the scale invariance of the model and reduce the parameter to a minimum of adimensional constants. All the polygons are supposed to have the same density. The mass m_i of each polygon is measured in units of the mean mass m_0 of the Voronoi tessellation. The time is measured in fractions of the total loading time t_0 . The evolution of the position \vec{x}_i and the orientation φ_i of the i -th polygon is governed by the equations of motion:

$$\begin{aligned} \lambda^2 m_i \ddot{\vec{x}}_i + \sum_c \vec{f}_i^c + \sum_{c_b} \frac{\sigma_i^b}{k_n} \vec{f}_i^b &= 0 \\ \lambda^2 I_i \ddot{\varphi}_i + \sum_c \vec{\ell}_i^c \times \vec{f}_i^c + \sum_{c_b} \frac{\sigma_i^b}{k_n} \vec{\ell}_i^b \times \vec{f}_i^b &= 0 \end{aligned} \quad (3)$$

The sums go over all those particles and boundary segments that are in contact with the i -th polygon. The interparticle contact forces \vec{f}_i^c and boundary forces \vec{f}_i^b are given by:

$$\begin{aligned} \vec{f}_i^c &= (\delta_i^c + \lambda \gamma m v_n^c) \hat{n}_i^c + \zeta (\xi_i^c - \lambda \gamma m v_t^c) \hat{t}_i^c \\ \vec{f}_i^b &= N_i^b - \lambda \gamma m_i \vec{v}_i \end{aligned} \quad (4)$$

Here δ_i^c and ξ_i^c are the deformation length and the tangential displacement of the contact, which were defined in Sect. II A; σ_i^b is the stress applied on the boundary segment T_i^b , defined in Sect. II B. Artificial viscous terms must be included in Eq. (4) to keep the stability of the numerical solution and reduce the acoustic waves generated during the loading process. \vec{v}_i^c is the relative velocity at the contact (Eq. (2)) and $m = (1/m_i + 1/m_j)^{-1}$ is the effective mass of the two polygons in contact.

There are four microscopic parameters in the model: the viscosity γ , the ratio $\lambda = t_s/t_0$ between the characteristic period of oscillation $t_s = \sqrt{k_n/m_0}$ and the loading time t_0 , the friction coefficient μ , and the ratio $\zeta = k_t/k_n$ between the tangential k_t and normal k_n stiffness of the interparticle contacts.

The viscosity factor γ is related to the normal restitution coefficient [9]. It was taken large enough to have a high dissipation, but not too large to keep the numerical stability of the method. The ratio λ was chosen small enough in order to avoid rate-dependence in the strain response, as corresponds to the quasi-static approximation. Technically, that is done by looking for the value of λ such that a reduction of it by half makes a change of the strain response less than 5%.

The two parameters ζ and μ determine the constitutive response of the system. For example, the micro-mechanical analysis of the strain response shows that the Young's modulus and Poisson's ratio depend on ζ [11]. In the other hand, μ can be directly related to the friction angle of the material [12]. Although the study of the dependence of the constitutive response on those parameters is an important point, such quantities have been kept fixed in this work.

The boundary conditions yield more dimensional parameters. The initial height H_0 and width W_0 of the sample, and the characteristic length ℓ_0 of the polygons define two geometrical parameters, which are the shape ratio W_0/H_0 and the granularity ℓ_0/H_0 of the sample.

In order to keep overlaps much smaller than the characteristic area of the polygons. The ratio σ_i/k_n between the stress applied on the membrane and the stiffness of the contacts is restricted to small values. This was implemented by fixing the contact stiffness to a value closed to the experimental granular stiffness $k_n = 160 \text{ MPa}$. Then the stress is chosen in such way that it does not exceed 1% of this value.

adimensional variable	ratio	default value
viscosity	γ	0.1
friction coefficient	μ	0.25
time's ratio	$\lambda = t_s/t_0$	8.0×10^{-4}
stiffness ratio	$\xi = k_t/k_n$	0.33
granularity	ℓ_0/H_0	0.1
shape ratio	W_0/H_0	1.0
bending angle	θ_{th}	0.25π

III. STRESS-STRAIN CALCULATION

A. Theoretical background

The macroscopic state of the system is characterized by the stress tensor and the void ratio e . The area fraction of voids in the sample defines the void ratio. Initially $e_0 = 0$ due to the Voronoi tessellation used. The stress controlled test was restricted to stress states without-off diagonal components. The diagonal component, the axial δ_1 and lateral δ_3 stress, define the stress vector:

$$\tilde{\sigma} = \begin{bmatrix} p \\ q \end{bmatrix} = \frac{1}{2} \begin{bmatrix} \delta_1 + \delta_3 \\ \delta_1 - \delta_3 \end{bmatrix} \quad (5)$$

where p and q are the pressure and the shear stress. The domain of admissible stresses is bounded by the failure surface. When the system reaches this surface it becomes unstable and fails.

Before failure, the constitutive behavior can be obtained performing small changes in the stress and evaluating the resultant deformation. An infinitesimal change of the stress vector $d\tilde{\sigma}$ produces an infinitesimal deformation of the sample, which is given by a change of height dH and width dW . This defines the axial strain $d\epsilon_1 = dH/H$ and lateral strain $d\epsilon_3 = dW/W$ increments. The volumetric strain $d\epsilon_v$ and the shear strain $d\epsilon_\gamma$ increments define the incremental strain vector:

$$d\tilde{\epsilon} = \begin{bmatrix} d\epsilon_v \\ d\epsilon_\gamma \end{bmatrix} = \begin{bmatrix} d\epsilon_1 + d\epsilon_3 \\ d\epsilon_1 - d\epsilon_3 \end{bmatrix} \quad (6)$$

Each state of the sample is related to a single point in the stress space, and the quasi-static evolution of the system is represented by the movement of this point in the stress space. The constitutive relation is formulated taking the incremental strain as a function of the incremental stress and the stress state.

$$d\tilde{\epsilon} = \mathcal{F}(d\tilde{\sigma}, \tilde{\sigma}) \quad (7)$$

If there is no rate - dependence in the constitutive equation, $\mathcal{F}(d\tilde{\sigma})$ is an homogeneous function of degree one. In this case, the application of the Euler identity [3] shows that Eq. (7) can be reduced to.

$$d\tilde{\epsilon} = M(\hat{\theta}, \tilde{\sigma})d\tilde{\sigma} \quad (8)$$

Where $\hat{\theta}$ is the unitary vector defining a specific direction in the stress space:

$$\hat{\theta} = \frac{d\tilde{\sigma}}{|d\tilde{\sigma}|} \equiv \begin{bmatrix} \cos \theta \\ \sin \theta \end{bmatrix}, \quad |d\tilde{\sigma}| = \sqrt{dp^2 + dq^2} \quad (9)$$

The constitutive relation results from the calculation of $d\tilde{\epsilon}(\theta)$, where each value of θ is related to a particular mode of loading. Some special modes are listed in the table:

0°	isotropic compression	$dp > 0 \quad dq = 0$
45°	axial loading	$d\sigma_1 > 0 \quad d\sigma_3 = 0$
90°	pure shear	$dp = 0 \quad dq > 0$
135°	lateral loading	$d\sigma_1 = 0 \quad d\sigma_3 > 0$
180°	isotropic expansion	$dp < 0 \quad dq = 0$
225°	axial stretching	$d\sigma_1 < 0 \quad d\sigma_3 = 0$
270°	pure shear	$dp = 0 \quad dq < 0$
315°	lateral stretching	$d\sigma_1 = 0 \quad d\sigma_3 < 0$

The relation (8) has been proposed by Darve [3], and it contains all the possible constitutive equations. In order to interpret our particular results, it is convenient to make some approximations: First, if the load increments are taken small enough, the tensor $M(\theta)$ can be supposed to be lineal in each stress direction. Then, we assume that the strain can be separated in an elastic (recoverable) and a plastic (unrecoverable) component:

$$d\tilde{\epsilon} = d\tilde{\epsilon}^e + d\tilde{\epsilon}^p \quad (10)$$

$$d\tilde{\epsilon}^e = D(\tilde{\sigma})d\tilde{\sigma} \quad (11)$$

$$d\tilde{\epsilon}^p = J(\theta, \tilde{\sigma})d\tilde{\sigma} \quad (12)$$

Here, D^{-1} defines the stiffness tensor, and $J = M - D$ the flow rule of plasticity, which results from the calculation of $d\tilde{\epsilon}^e(\theta)$ and $d\tilde{\epsilon}^p(\theta)$.

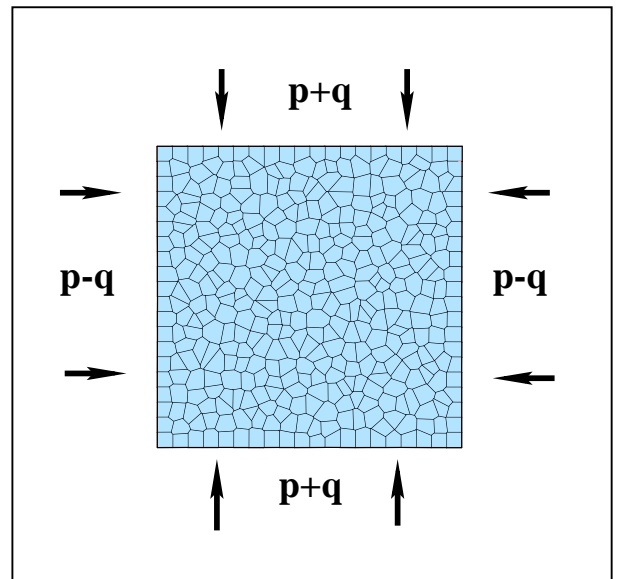


FIG. 4. Axial stress $\sigma_1 = p + q$ and lateral stress $\sigma_3 = p - q$ in a stress controlled test. They are applied on the boundary of the tessellated sample of polygons.

B. The method

A numerical method has been implemented in order to find the elastic $d\tilde{\epsilon}^e$ and plastic $d\tilde{\epsilon}^p$ components of the strain as function of the stress state $\tilde{\sigma}$ and the stress direction θ . Fig. 5 shows the three steps of the procedure:

1) The sample is driven to the stress state $\tilde{\sigma}$. First, it is isotropically compressed until it reaches the stress value $\delta_1 = \delta_3 = p - q$. Next, it is subjected to axial loading, in order to increase the axial stress δ_1 until $p + q$ (see Fig. 4). When the stress state $\tilde{\sigma} = [p \ q]^T$ is reached, (A^T being the transpose of A) the sample is allowed to relax.

2) Loading the sample from $\tilde{\sigma}$ to $\tilde{\sigma} + d\tilde{\sigma}$ the strain increment $d\tilde{\epsilon}$ is obtained. This procedure is implemented choosing different stress directions according to Eq. (9). Here the stress modulus is fixed to $|d\tilde{\sigma}| = 10^{-4}p$.

3) The sample is unloaded until the original stress state $\tilde{\sigma}$ is reached. Then one finds a remaining strain $d\tilde{\epsilon}^p$, that corresponds to the plastic component of the incremental strain. Since the stress increments are taken small enough, the unloaded stress-strain path is practically elastic. Thus, the difference $d\tilde{\epsilon}^e = d\tilde{\epsilon} - d\tilde{\epsilon}^p$ represents the elastic component of the strain.

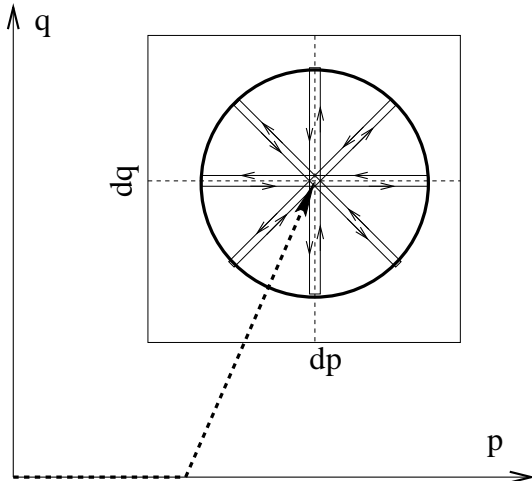


FIG. 5. Procedure to obtain the constitutive behavior: 1) The sample is driven to the stress state $\tilde{\sigma}$, with pressure p and shear stress q . 2) It is loaded from $\tilde{\sigma}$ to $\tilde{\sigma} + d\tilde{\sigma}$ 3) It is unloaded to the original stress state $\tilde{\sigma}$.

One could be concerned about the dependence of the strain response on the way how the stress state is reached. We found that there is not remarkable dependence of the strain response on the stress path, whenever the stress components are quasi - static and monotonically increased. Otherwise, a strong reduction in the plastic component of the strain is observed. In fact, when the plastic response is calculated after the sample is unloaded, the plasticity results smaller than that one calculated after a monotonic load. Furthermore, there is

no plastic component in the strain response when elastic waves are previously generated in the sample. Those memory effects suggest that the plastic component of the strain depend on the history of the deformation, and is kept unchanged only if the sample is subjected to quasi-static and monotonic load.

Fig. 6 shows the load-unload paths and the corresponding strain response. They were taken from a stress-state with $q = 0.5p$. The end of the load paths in the stress space map into a strain envelope response $d\tilde{\epsilon}(\theta)$ in the strain space. Likewise, the end of the unload paths map into a plastic envelope response $d\tilde{\epsilon}^p(\theta)$. The yield direction ϕ can be found from this response, as the direction in the stress space where the plastic response is maximal. The flow rule can be obtained taking the direction ψ of the maximal plastic response in the strain space. These angles do not agree, that reveals the necessity to analyze this behavior in the framework of the non-associated theory of plasticity (see Sect. IV C).

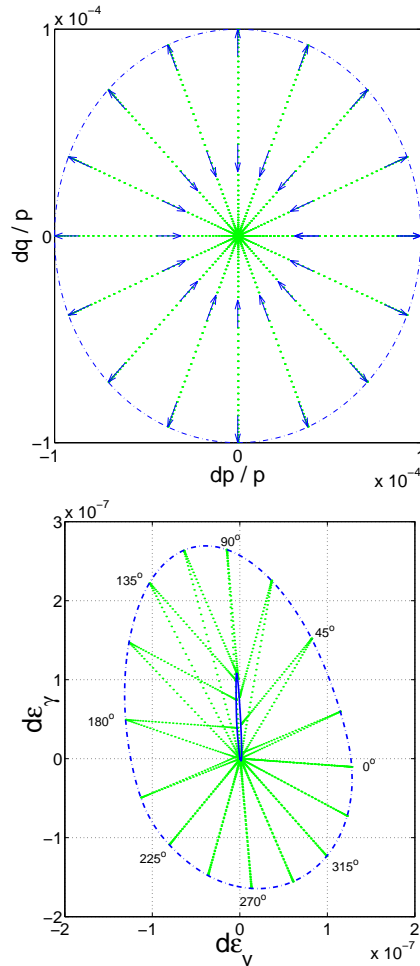


FIG. 6. Stress - strain relation resulting from the load - unload test. Dotted lines represent the paths in the stress and strain spaces. The dash-dot line gives the strain envelope response and the solid line is the plastic envelope response.

IV. CONSTITUTIVE RELATION

Fig. 7 summarizes the global elasto-plastic behavior. The elastic response, calculated from Eq. (10), has a centered ellipse as envelope response. This can be related to the micro-contact structure using a local linear relation in each point of the stress space (see Sect. IV B). The solid line represents the failure surface, which separates the stable states of the unstable ones (see Sect. IV A). The plastic envelope response is almost on a straight line. The modulus and the orientation of this envelope depend on the stress state through a certain number of material parameters, which are given in Sect. IV C. All the quantities obtained in this section have been calculated from the average over five different samples of 10×10 particles each one.

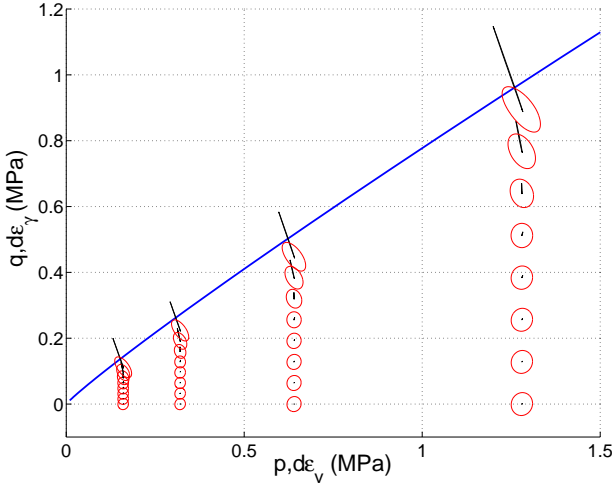


FIG. 7. Elastic response $d\epsilon^e$ and plastic response $d\epsilon^p$ resulting from the application of different loading modes with $|d\tilde{\sigma}| = 10^{-4}p$. The solid line represents the failure surface.

A. Failure surface

The failure line was calculated looking for the values of stress for which the system becomes unstable: for each pressure p , there is a critical shear stress $q_c(p)$, below which the sample reaches a stable state with an exponential decay of its kinetic energy. For shear stress values above the critical one, the sample develops an instability and fails. Fig. 8 shows the interface between these two stress states, that can be accurately fitted by the power law:

$$\frac{q_c}{p_0} = \mu^* \left(\frac{p}{p_0} \right)^\beta \quad (13)$$

Here $p_0 = 1.0 \text{ MPa}$ is the reference pressure, and $\mu^* = 0.78 \pm 0.03$ is the Mohr-Coulomb friction coefficient [1].

The power law dependence on the pressure, with exponent $\beta = 0.92 \pm 0.02$ implies a significant deviation from the Mohr-Coulomb theory. Moreover, the empirical criteria of failure for most rocks [15] shows a power law dependence of the form of Eq. (13). It seems that additional features beyond the Mohr-Coulomb analysis are taking place when the sample fails, that will be discussed in sect. IV C.

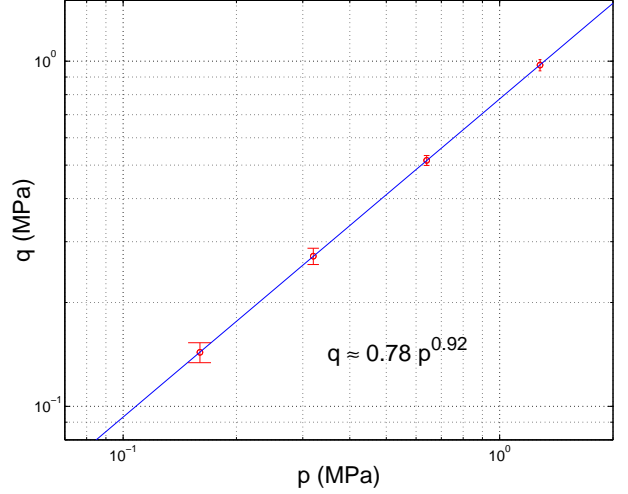


FIG. 8. Failure surface. The continuous line represents the power law fit.

B. stiffness

Hooke's law of elasticity states that the stiffness tensor of isotropic materials can be written in terms of two material parameters: the Young's modulus E and the Poisson's ratio ν . However, the isotropy is not fulfilled when the stress state is far from the hydrostatic axis. Indeed, numerical simulations [16,17] and photo-elastic experiments [18] on granular materials show that the loading induces a significant departure from isotropy in the contact network.

The anisotropy of the granular sample can be characterized by the distribution of the micro-contact normal vectors \hat{n}_i^φ (see Fig. 1). Our numerical simulations show that the structural changes of micro-contacts are principally due to the opening of contacts whose normal vectors are nearly aligned around the direction perpendicular to the load. Let us call $N(\varphi)\Delta\varphi$ the number of contacts per particle, oriented between the angles φ and $\varphi + \Delta\varphi$, measured with respect to the direction in which the sample is loaded. The lowest order of anisotropy can be described by:

$$N(\varphi) = \frac{1}{2\pi} [N + (N_0 - N) \cos(2\varphi)] \quad (14)$$

Here N is the average coordination number of the polygons, whose initial value $N_0 = 6.0$ reduces as the load is

increased. Fig. 9 shows this reduction. A critical line is found around $q = 0.12p$, below which there are no structural changes in the contact network. Above this limit an induced anisotropy arises due to opened contacts whose amount follows a power law dependence.

In order to describe the effect of the anisotropy in the elastic response we proceed as follows: first, an additional parameter α is included in Hooke's law

$$\begin{bmatrix} d\epsilon_1^e \\ d\epsilon_3^e \end{bmatrix} = \frac{1}{E} \begin{bmatrix} 1-\alpha & -\nu \\ -\nu & 1+\alpha \end{bmatrix} \begin{bmatrix} d\sigma_1 \\ d\sigma_3 \end{bmatrix} \quad (15)$$

Then, these three parameters are supposed to be depended on the internal damage parameter d :

$$d = \frac{N_0 - N}{N_0} \quad (16)$$

The tensor D defined in Eq. (11) is calculated from Eq. (15) using the definition of the stress and strain vectors given in Eqs. (5) and (6). One obtains:

$$D = \frac{2}{E} \begin{bmatrix} 1-\nu & -\alpha \\ -\alpha & 1+\nu \end{bmatrix} \quad (17)$$

The diagonal components of this tensor are respectively the inverse of the bulk modulus and of the shear modulus. The non-diagonal component results from the anisotropy of the sample, and it couples the compression mode with the shearing deformation. These three variables are calculated from the elastic response $d\tilde{\epsilon}^e(\theta)$ by the introduction of the following function:

$$R(\theta) = \frac{d\tilde{\sigma}^T d\tilde{\epsilon}^e}{|d\tilde{\sigma}|^2} \quad (18)$$

by substitution of Eqs. (11) and (9) into Eq. (18), one sees that R is the quadratic form of D :

$$R(\theta) = \hat{\theta}^T D \hat{\theta} = \frac{2}{E} [1 - \nu \cos(2\theta) - \alpha \sin(2\theta)] \quad (19)$$

Using this equation, the components of D can be evaluated as the Fourier coefficients of R :

$$\frac{1}{E} = \frac{1}{4\pi} \int_0^{2\pi} R(\theta) d\theta \quad (20)$$

$$\nu = -\frac{E}{2\pi} \int_0^{2\pi} R(\theta) \cos(2\theta) d\theta \quad (21)$$

$$\alpha = -\frac{E}{2\pi} \int_0^{2\pi} R(\theta) \sin(2\theta) d\theta \quad (22)$$

Figs. 10, 11 and 12 show the results of the calculation of the Young's modulus E , the Poisson's ratio ν and the anisotropy factor α . Below the limit of isotropy, Hooke's law can be applied: $E \approx E_0$, $\nu \approx \nu_0$ and $\alpha \approx 0$. On the other hand, above the limit of isotropy a reduction of the Young's modulus is found, along with an increase of the Poisson's ratio and the anisotropy factor. The functional

dependence of those parameters with the internal damage parameter d are evaluated developing their Taylor's series around $d = 0$:

$$\begin{aligned} E(d) &= E(0) + E'(0)d + O(d^2) \\ \alpha(d) &= \alpha(0) + \alpha'(0)d + O(d^2) \\ \nu(d) &= \nu(0) + \nu'(0)d + \nu''(0)d^2 + O(d^3) \end{aligned} \quad (23)$$

The coefficients of this expansion are calculated from the best fitting of those expansions. Figs. 10 and 12 show that the linear approximation is good enough to reproduce the Young's modulus and the anisotropy factor. The fit of the Poisson's ratio, however, requires the inclusion of a quadratic approximation, implying that it has a non-linear dependence on the damage parameter (Fig. 11).

C. Plastic Flow

The formulation of the non-associated theory of plasticity requires the evaluation of three material functions: the yield direction ϕ , the flow direction ψ , and the plastic modulus h . These quantities can be calculated from the plastic response $d\tilde{\epsilon}^p(\theta)$, as follows:

The yield direction is given by the incremental stress direction ϕ with maximal plastic response:

$$|d\tilde{\epsilon}^p(\phi)| = \max_{\theta} |d\tilde{\epsilon}^p(\theta)| \quad (24)$$

The flow direction is defined from the orientation of the plastic response at its maximum value:

$$\psi = \arctan\left(\frac{d\epsilon_1^p}{d\epsilon_3^p}\right) |_{\theta=\phi} \quad (25)$$

The plastic modulus is obtained from the modulus of the maximal plastic response:

$$\frac{1}{h} = \frac{|d\tilde{\epsilon}^p(\phi)|}{|d\tilde{\sigma}|} \quad (26)$$

Reciprocally, the plastic response can be expressed in terms of these quantities. Let us define the unitary vectors $\hat{\psi}$ and $\hat{\psi}^\perp$. The first one is oriented in the direction of ψ and the second one is the 90° rotation of $\hat{\psi}$. The plastic strain is written in this basis as:

$$\begin{aligned} d\tilde{\epsilon}^p(\theta) &= [(d\tilde{\epsilon}^p)^T \hat{\psi}] \hat{\psi} + [(d\tilde{\epsilon}^p)^T \hat{\psi}^\perp] \hat{\psi}^\perp \\ &\equiv \frac{1}{h} \left[f(\theta) \hat{\psi} + g(\theta) \hat{\psi}^\perp \right] \end{aligned} \quad (27)$$

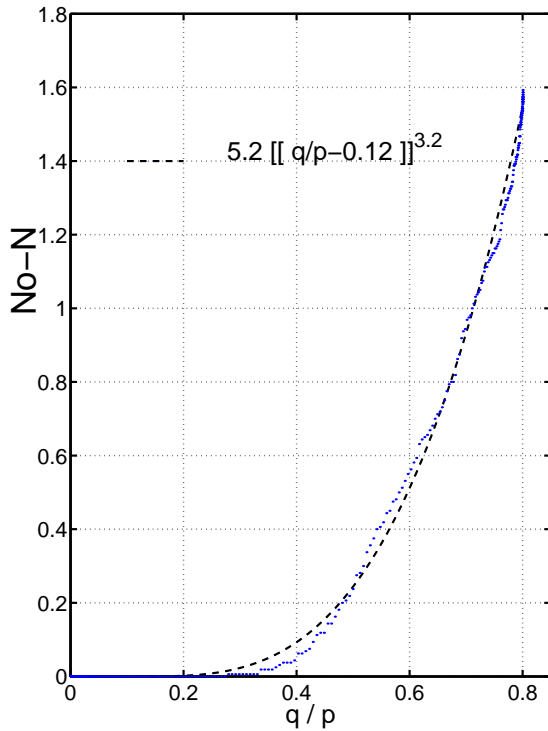


FIG. 9. Reduction of the mean coordination number of contacts (dotted line). The data have been fitted to a truncated power law (dashed line). See Eq. (29).

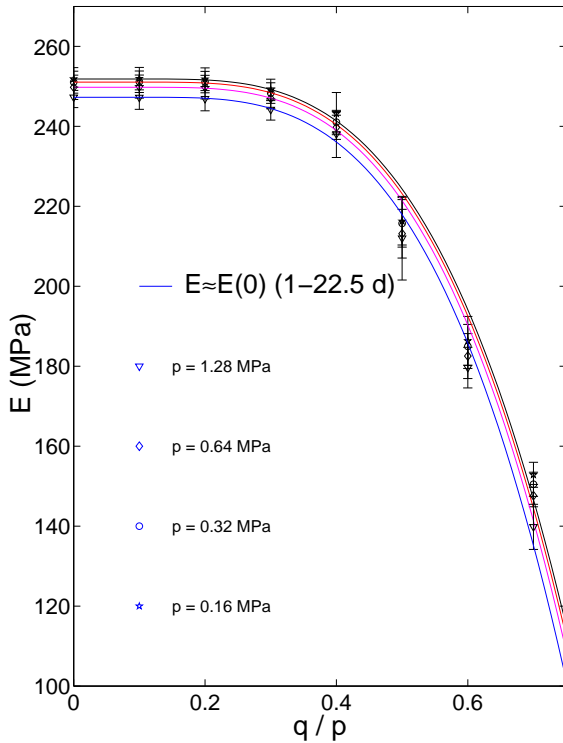


FIG. 10. Young's modulus. The solid line is the linear approximation of $E(d)$. See Eq. (24).

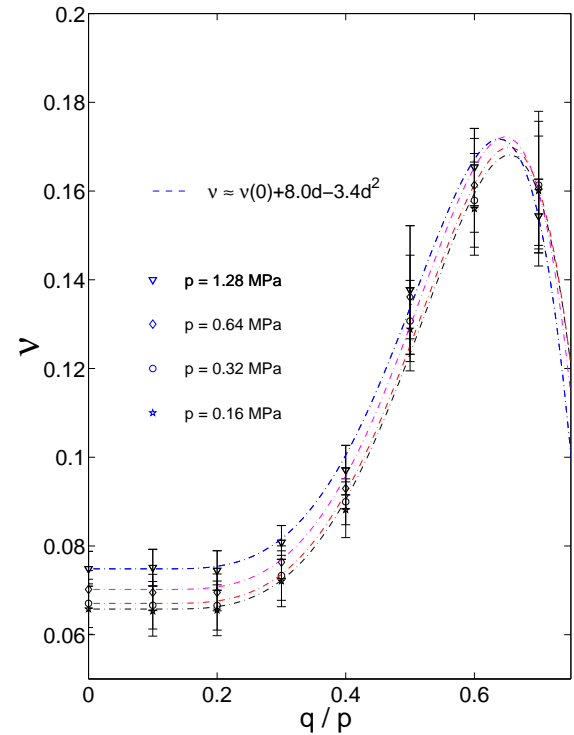


FIG. 11. Poisson's ratio. The dashed line is the quadratic approximation of $\nu(d)$. See Eq. (24).

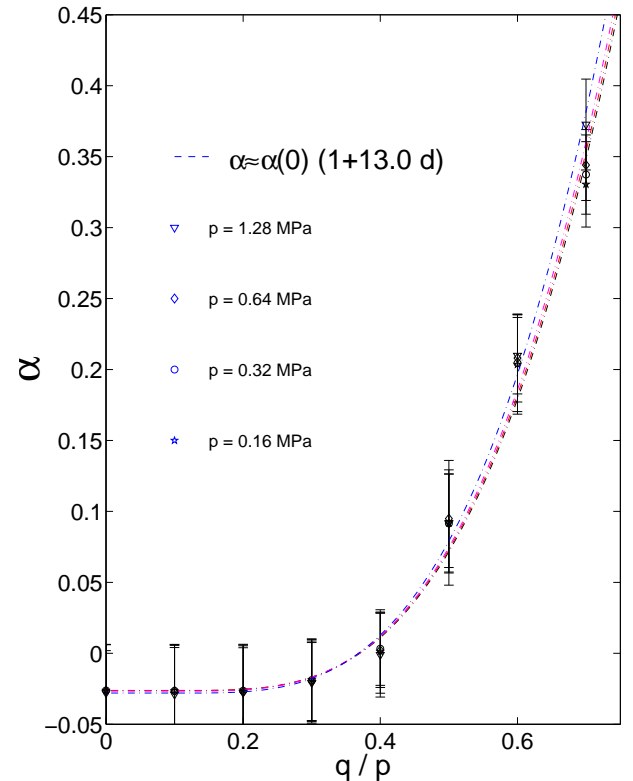


FIG. 12. Anisotropy parameter. The dashed line is the linear approximation of $\alpha(d)$. See Eq. (24).

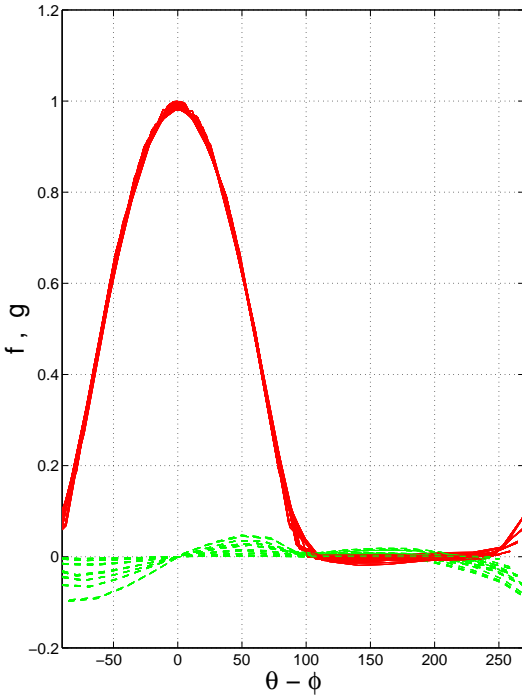


FIG. 13. Plastic profiles $f(\theta)$ (solid line) and $g(\theta)$ (dashed line). The results for different stress values have been superposed.

The plastic profiles $f(\theta)$ and $g(\theta)$ are shown in Fig. 13. The first one is approximately the same for all the stress states, and can be well fitted to a cosine function, centered on the yield direction ϕ and truncated to zero for the negative values. The last profile depends on the stress value, and is difficult to evaluate, because it is of the same order as the statistical fluctuations. However, the contribution of g to the total strain response is negligible. In order to simplify the description of the plastic response, the following approximation is made:

$$g(\theta) \ll f(\theta) \approx [[\cos(\theta - \phi)]] = [[\hat{\phi}^T \hat{\theta}]] \quad (28)$$

where $[[\cdot]]$ defines the function

$$[[x]] = \begin{cases} 0 & : x \leq 0 \\ x & : x > 0 \end{cases} \quad (29)$$

Now, The flow rule results from the substitution of Eqs.(27) and (28) into Eq. (12):

$$J(\theta)d\tilde{\sigma} = \frac{[[\hat{\phi}^T d\tilde{\sigma}]]}{h} \hat{\psi} \quad (30)$$

The yield direction and the flow direction have been calculated for different stress states. The results are shown in Fig. 14. Both angles are quite different, which is a clear deviation from Drucker's normality postulate [13]. Indeed, many experimental results on soil deformation [14] have confirmed that these angles are completely different. Thus Drucker's postulate is not fulfilled in the

deformation of granular materials, and the main reason for that is the rearrangement of contacts on small deformations which are not taken into account in this theory. On the other hand, all the sliding, opening, and other micro-mechanical rearrangements can be well handled in the discrete element formulation, which results more adequate to describe the soil deformation.

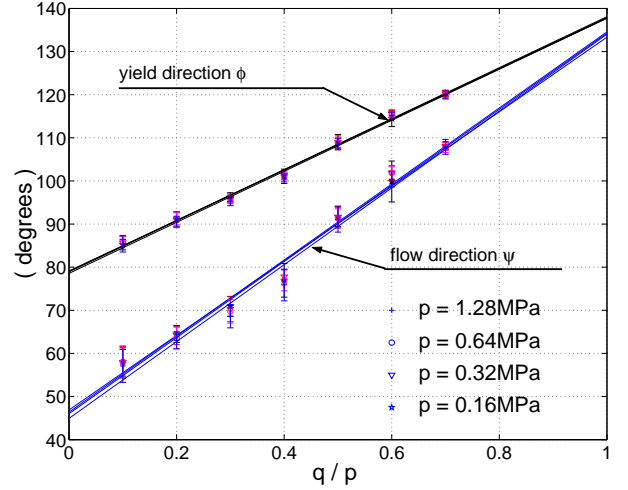


FIG. 14. The flow direction and the yield direction of the plastic response. Solid lines represent a linear fit.

The material constants are evaluated from the dependence of the plastic quantities on the stress: the yield direction and the flow direction can be roughly approximated by straight lines:

$$\begin{aligned} \phi &= \phi_0 + \phi'_0 \frac{q}{p} \\ \psi &= \psi_0 + \psi'_0 \frac{q}{p} \end{aligned} \quad (31)$$

The four material parameters $\phi_0 = 46^\circ \pm 0.75^\circ$, $\phi'_0 = 88.3^\circ \pm 0.6^\circ$, $\psi_0 = 78.9^\circ \pm 0.2^\circ$ and $\psi'_0 = 59.1^\circ \pm 0.4^\circ$ are obtained from the linear fit of the data. On the other hand, Fig. 15 shows that the plastic modulus depends on the stress through a power law relation:

$$h = h_0 \left[1 - \frac{q}{\mu^* p_0} \left(\frac{p_0}{p} \right)^\vartheta \right]^\eta \quad (32)$$

There are four additional material parameters: The plastic modulus $h_0 = 14.5 \pm 0.05$ at $q = 0$, the Mohr-Coulomb friction coefficient μ^* (see Eq. (13)), and the exponents $\eta = 2.7 \pm 0.04$ and $\vartheta = 0.981 \pm 0.002$.

The plastic limit surface is given by the stress states where the plastic deformation becomes infinite. According to the flow rule (Eq. (30)), it is found looking for the stress values where Eq. (32) vanishes:

$$\frac{q_p}{p_0} = \mu^* \left(\frac{p}{p_0} \right)^\vartheta \quad (33)$$

It is important to point out that the failure surface –given in Eq. (13)– does not correspond to the plastic limit surface. Actually, This matter has already been discussed in the framework of the Hill’s condition of instability [19] the bifurcation analysis [20], which predict that the instability should be reached strictly inside the plastic limit surface.

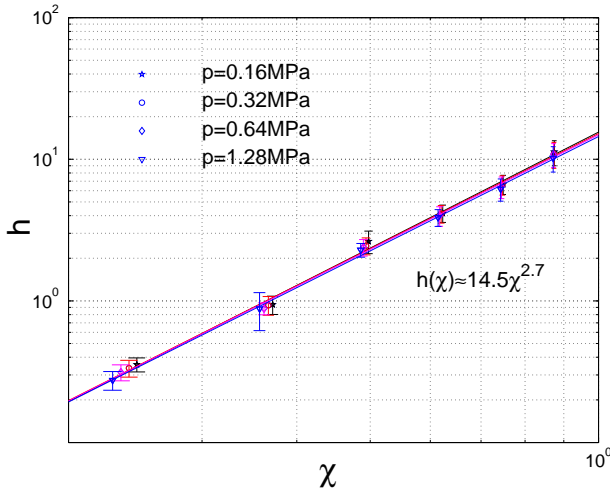


FIG. 15. Plastic modulus. The solid line is a power law fit with respect to the variable $\chi = 1 - (p/p_0)^q / (\mu^* p_0)$.

V. CONCLUDING REMARKS

The elasto-plastic response of a Voronoi tessellated sample of polygons has been calculated in the case of monotonic and quasi-static loading. It can be written in a simple form as:

$$d\tilde{\epsilon} = D(d)d\tilde{\sigma} + \frac{[[\hat{\phi}^T d\tilde{\sigma}]]}{h}\hat{\psi} \quad (34)$$

The plastic response reflects the non-associated features of realistic soils. Here the yield direction and flow direction are linearly related to the ratio q/p , and the plastic modulus obeys a power law relation with a weak pressure dependence.

The classical parameters of elasticity – the Young’s modulus and the Poisson’s ratio – are not material constants, because they depend on the internal damage parameter. Therefore, Eq. (34) is not complete, and it is necessary to include a constitutive equation that relates the internal damage to the external load. By focusing on the details of the dynamic of the micro-contacts, significant progress may be made in the macroscopic description of the deformation.

The elasto-plastic response leads to the identification of three different regimes which are shown in Fig. 16. Zone I corresponds to the isotropic regime, characterized by small plastic deformations and a linear elastic regime.

In the zone II open contacts are detected, which must be taken into account in the calculation of the non linear elasticity. Zone III corresponds to unstable states so that the stress-strain relation can not be calculated here. The extrapolation of the strain response in this region shows that the plastic strain must have a finite value just before the instability is reached.

The above observation leads to the open question of the nature of the failure [19]. Numerical simulations on strain controlled tests show that strain localization is the most typical mode of failure. The fact that it appears before the sample reaches the plastic limit surface suggests that the appearance of the instability is not completely determined by the macroscopic state.

The role of the microstructure on the strain localization has been intensely studied in the last years [20,21]. Future work is the creation of samples with different granular textures –for example, changing the void ratio distributions and the polydispersity of the grains–. Then we can deal with the question of how a change in the microstructure affects the elasto-plastic response and the strain localization.

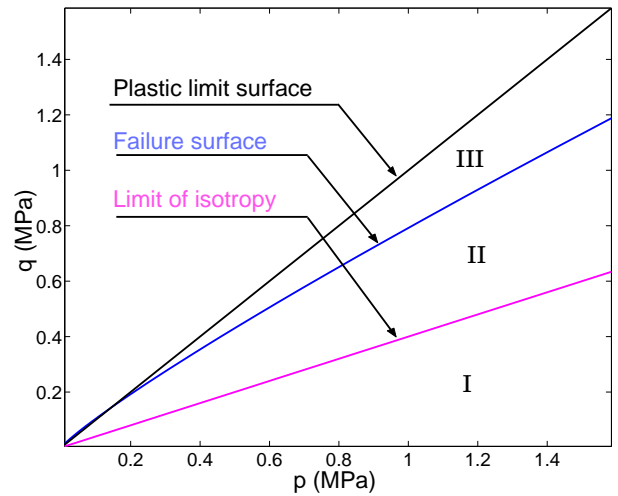


FIG. 16. Elasto-plastic regimes: isotropic(I), anisotropic (II) and unstable (III).

ACKNOWLEDGMENTS

We thank F. Darve, P. Vermeer, F. Kun, J. Åström and S. Luding for helpful discussions and acknowledge the support of the *Deutsche Forschungsgemeinschaft* within the research group *Modellierung kohäsiver Reibungsmaterialien*.

- [1] P. A. Vermeer, *A five-constant model unifying well-established concepts Constitutive Relations of soils* . Edited by G. Gudehus, F. Darve and L. Vardoulakis, Balkema Rotterdam, 175-197 (1984)
- [2] D. Kolymbas *An outline of hypoplasticity* Archive of Applied Mechanics 61, 143-151 (1991)
- [3] F. Darve, *Incremental non-lineal constitutive relationships* Geomaterials Constitutive Equations and Modeling, edited by F. Darve, Elsevier applied Science, London 123-148 (1990)
- [4] P.A Cundall, *Numerical experiments on localization in frictional materials* Ingenieur-Archiv, 59 879-908 (1989)
- [5] J.P. Bardet, *Numerical solutions of incremental response of idealized granular materials* International Journal of Plasticity 10(8) 879-908 (1994)
- [6] H. Tillemans and H.J. Herrmann, *Simulating deformations of granular solid under shear* Physica A 217, 261-288 (1995)
- [7] F. Kun and H.J. Herrmann, *A study of fragmentation process using a discrete element method* Computational Methods in Applied Mechanics and Engineering 138, 3-18 (1996)
- [8] L. Brendel and S. Dippel *Lasting contacts in molecular dynamics simulations* in Proceedings of Physics of Dry Granular Media, NATO ASI Series E 350, Edited by H.J. Herrmann, J.-P. Hovi and S. Luding, Kluwer Academic Publishers, 313-318 (1998)
- [9] S. Luding, *Collisions & contacts between two particles* Proceedings of Physics of Dry Granular Media, NATO ASI Series E 350, Edited by H. J. Herrmann, J.-P. Hovi and S. Luding, Kluwer Academic Publishers, 285-304 (1998)
- [10] J. A. Åström , H.J.Herrmann and J. Timonen, *Granular Packings and Fault Zones* Physical Review Letters 84, 4 638-641 (2000)
- [11] N.P. Kruyt and L. Rothenburg, *Micro-mechanical Definition of the strain tensor for granular materials* Journal of Applied Mechanics 118, 706-719 (1996)
- [12] L. Oger, S.B. Savage, D.Corriveau and M. Sayed, *Yield conditions of an assembly of disk subjected to a deviatoric stress* Powders & Grains 97, edited by Behringer and Jenkins 283-286 (1997)
- [13] D.C. Drucker and W. Prager. *Soil Mechanics and plastic analysis of limit design* Q. Applied Math. 10(2) 157-165 (1952)
- [14] F. Tatsuoka and K. Ishihara, *Yielding of sand in triaxial compression* Soil and Foundations 14, 2 63-76 (1974)
- [15] N.G.W. Cook and K. Hodgson *Some detailed stress - strain curves for Rock* J. Geophys. Research 70, 2883-2888 (1965)
- [16] C. Thornton *Computer simulated deformation of compact granular assemblies* Acta Mechanica 64, 45-61 (1986)
- [17] M. Lätsel, S. Luding, and H. J. Herrmann, *Macroscopic material properties from quasi-static, microscopic simulations of a two-dimensional shear-cell* Granular Matter 2(3), 123-135, (2000)
- [18] M. Oda. J. Konishi and S. Nemat-Nasser, *Experimental micro-mechanical evaluation of strength of granular materials: effect of particle rolling* Mech. Mater 1, 267-283 (1982)
- [19] F.Darve and F. Laouafa, *Instabilities in granular materials and application to landslides* Mechanics of Cohesive-Frictional Materials 5, 627-652 (2000)
- [20] I. Vardoulakis, J. Sulem. *Bifurcation Analysis in Geomechanics* Blackie Academic & Professional, (1995)
- [21] G. Viggiani, M. Küntz and J. Desrues, *An experimental investigation of the relationship between grain size distribution and shear banding in sand* Continuous and Discontinuous Modeling of Cohesive-Frictional Materials, Edited by P.A. Vermeer, H.J.Herrmann, E.Ramm W. Ehlers, Springer, Lectures notes in Physics 568, 111-127 (2001)